

Supplementary Information

Mesoporous Nitrogen-doped Carbon from Nanocrystalline Chitin Assemblies

Thanh-Dinh Nguyen, Kevin E. Shopsowitz, and Mark J. MacLachlan*

Department of Chemistry, University of British Columbia,
2036 Main Mall, Vancouver, British Columbia, Canada V6T 1Z1

E-mail: mmaclach@chem.ubc.ca

Experimental Section

Starting Materials: King crab shells were obtained from *Paralithodes camtschaticus* species in local seafood markets. Tetramethoxysilane ($\text{Si}(\text{OCH}_3)_4$, 99%) was purchased from Acros chemicals and used as received without further purification. Other chemicals, including sodium hydroxide, hydrochloric acid, and hydrogen peroxide, were obtained from standard suppliers. Purification of chitin fibrils from king crab shells and preparation of aqueous suspensions of nematic nanocrystalline chitin by sequential deacetylation and hydrolysis of the fibrils were achieved as described in our previous report.¹ The chitin nanocrystals prepared by this two-step method gave a positive surface charge of the free primary amine groups (zeta potential of 43.1 ± 1.7 mV) higher than those obtained by only acid hydrolysis, resulting in the ordered nematic organization of the chitin assemblies.

Characterization: Powder X-ray diffraction (PXRD) patterns of the samples were recorded on a D8 advance X-ray diffractometer. Raman spectroscopy were collected using a SpectraCode model RP-1 spectrometer with a 785 nm excitation. XPS measurement was achieved in an ion-pumped chamber (evacuated to 10^{-9} Torr) of a photoelectron spectrometer (Kratos Axis-Ultra)

equipped with a focused X-ray source (Al K_{α} , $h\nu = 1486.6$ eV). The binding energy of the samples was calibrated by setting the C 1s peak to 285 eV. The peaks were deconvoluted by means of a standard CasaXPS software (v.2.3.13; product of CasaXPS Software Ltd., USA) to resolve the separate constituents after background subtraction. Scanning electron microscopy (SEM) images were obtained on a Hitachi S4700 electron microscope. Samples were prepared by breaking films into small pieces and attaching them to aluminum stubs using double-sided adhesive tape and were then sputter-coated with gold-palladium (5 nm). Transmission electron microscopy (TEM) images of the samples were obtained on a Hitachi H7600 electron microscope. The nanocrystalline chitin samples were prepared by placing one droplet (0.1 mL) of the diluted NCh solution (0.0005 wt%) on a carbon-coated copper grid after sonicating for at least 20 min and then dried at ambient conditions. To image the carbon-based films, samples were gently ground to a fine powder, suspended in ethanol, then deposited on the TEM grid. Polarized optical microscopy (POM) was performed on an Olympus BX41 microscope. Thermogravimetric analysis (TGA) of the carbon-based films (~1.0 mg) was conducted at a heating rate of 10 °C min⁻¹ under air to 900 °C using a PerkinElmer Pyris 6 thermogravimetric analyzer. Infrared spectra were obtained on a Nicolet 6700 FT-IR spectrometer equipped with a Smart Orbit diamond attenuated total reflectance (ATR) attachment. Nitrogen adsorption-desorption isotherms were obtained using a Micromeritics Accelerated Surface Area & Porosity (ASAP) 2000 system; before measurements, the film samples (~100 mg) were degassed at 150 °C in vacuum for 4 h. Zeta potentials of the diluted NCh solution (0.01 wt%) with pH 4 were obtained using Zetasizer 3000 HS. CNH elemental analysis was obtained at the UBC Structural Analysis facility. EDX analysis was collected using a Hitachi S2300 scanning electron microscope.

The standard four-probe method was used to measure the electrical conductivity of the mesoporous nitrogen-doped carbon. Hewlett-Packard model 34401A and 3478A multimeters were used to measure the voltage and current. The temperature-dependent electrical conductivity was recorded by varying the temperature of a rectangular-shaped film placed on an insulated glass surface equipped with a temperature-controlled heater over a range of 25 to 180 °C. The electrochemical measurements were performed by two-electrode configuration using a Brinkmann PGSTAT12 Autolab potentiostat. Dried carbon-based mesoporous films were weighed and then soaked in a 1 M H₂SO₄ aqueous solution for at least 18 h. Two pieces of

symmetrical carbon-based mesoporous films, one piece of 110 mm-sized round Whatman filter paper, and 1 M H₂SO₄ have been used as electrodes, separator, and electrolyte, respectively. Stainless-steel collectors sandwiched two films with a filter paper separator and were placed in a Swagelok two-electrode cell.

Calculation of electrical conductivity

The electrical conductivity of the mesoporous nitrogen-doped carbon films was measured by using the standard four-probe method² based on equation 1:

$$\sigma = \frac{1}{\rho} = \frac{1}{4.5324t\left(\frac{V}{I}\right)f} \quad (\text{S cm}^{-1}) \quad (\text{Eqn 1})$$

where V (V) and I (A) are the recorded voltage and current, respectively. t is film thickness (mm), f is a function of the width and length of a rectangular-shaped film and of probe spacing, which was calculated based on a standard diagram describing the relationship between f and width/probe spacing. In our case, $f = 0.49$ as film width = 6.5 mm and probe spacing = 2.5 mm.

Calculation of specific capacitance (C_s)

C_s of the carbon-based mesoporous materials with respect to two-electrode full cell is derived from the cyclic voltammogram based on equation 2:

$$C_s = 2 \frac{I}{Vm} \quad (\text{F g}^{-1}) \quad (\text{Eqn 2})$$

where I (A), V (V), and m (g) are the current received from the charge scan of the CV curve, the voltage sweep rate, and the mass of the sample per electrode, respectively.

C_s of the supercapacitor electrodes can also be estimated from galvanostatic charge/discharge profile based on equation 3:

$$C_s = 2 \frac{I}{\left(\frac{dV}{dt}\right)m} \quad (\text{F g}^{-1}) \quad (\text{Eqn 3})$$

where I (A), dV/dt ($V s^{-1}$), and m (g) are the applied galvanostatic current, the slope of discharge curve when the charge/discharge curve is approximately linear and symmetric, and the mass of the sample per electrode, respectively.

Supplementary Figures

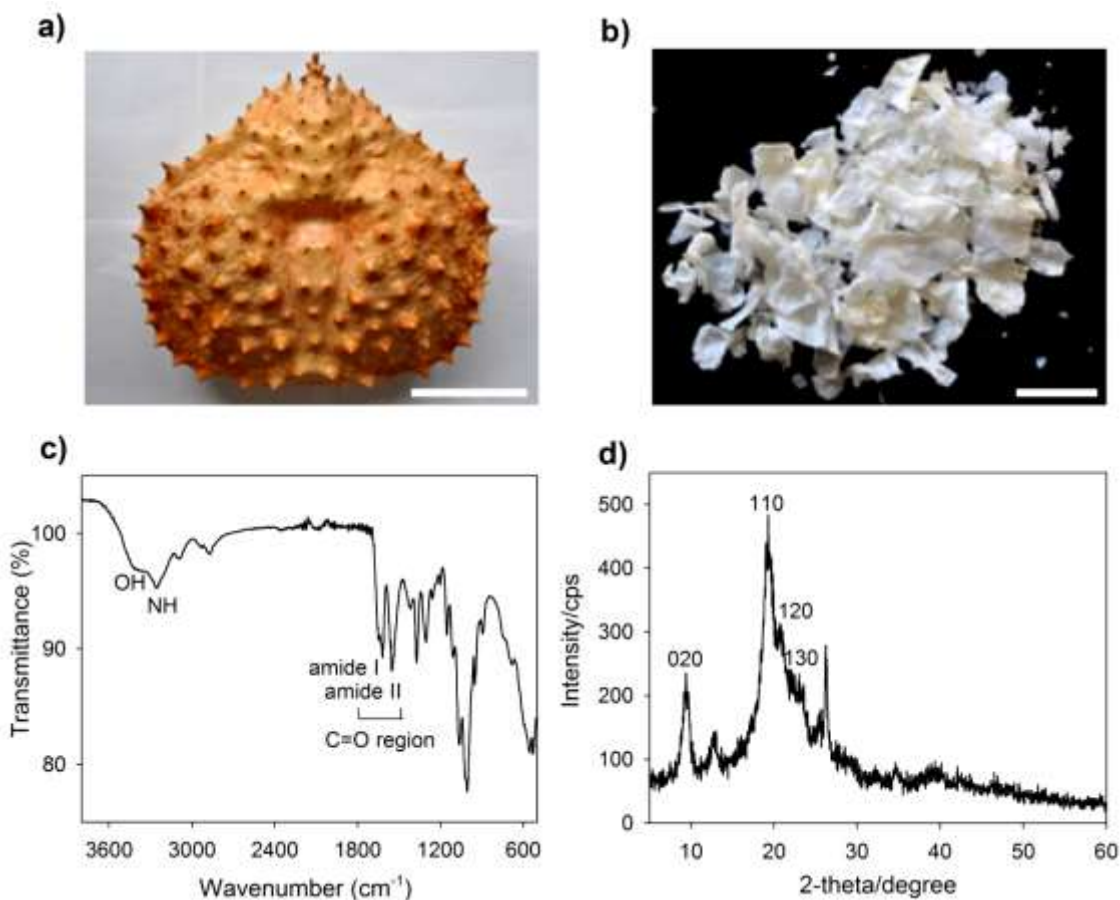


Figure S1. Preparation of the chitin nanocrystals from the king crab shells. (a) Dried king crab shells. (b) Pure chitin fibrils after removal of protein, minerals, and pigment. FTIR spectrum (c) and PXRD pattern (d) of the chitin nanocrystals prepared by sequential alkaline-treated deacetylation and hydrochloride acid-catalyzed hydrolysis of the chitin fibrils. FTIR spectrum of the chitin nanocrystals shows NH stretching band at 3270 cm⁻¹, amide band I at 1660 and 1620 cm⁻¹, amide II band at 1560 cm⁻¹ and OH stretching band at 3482 cm⁻¹ of the chitin. These strong absorption peaks in the carbonyl region are characteristic of anhydrous chitin molecules.³ PXRD pattern of the chitin nanocrystals shows diffraction peaks at 9.5, 19.5, 20.9, 23.4° 2θ corresponding to (020), (110), (120), (130) planes, which are characteristic of the α-chitin structure. The absence of a peak at 29.6° 2θ assigned to calcium carbonate revealed the thorough removal of the mineral components.³ These analyzed results demonstrate that the deacetylation and hydrolysis did not modify the original α-structure of the chitin fibers.

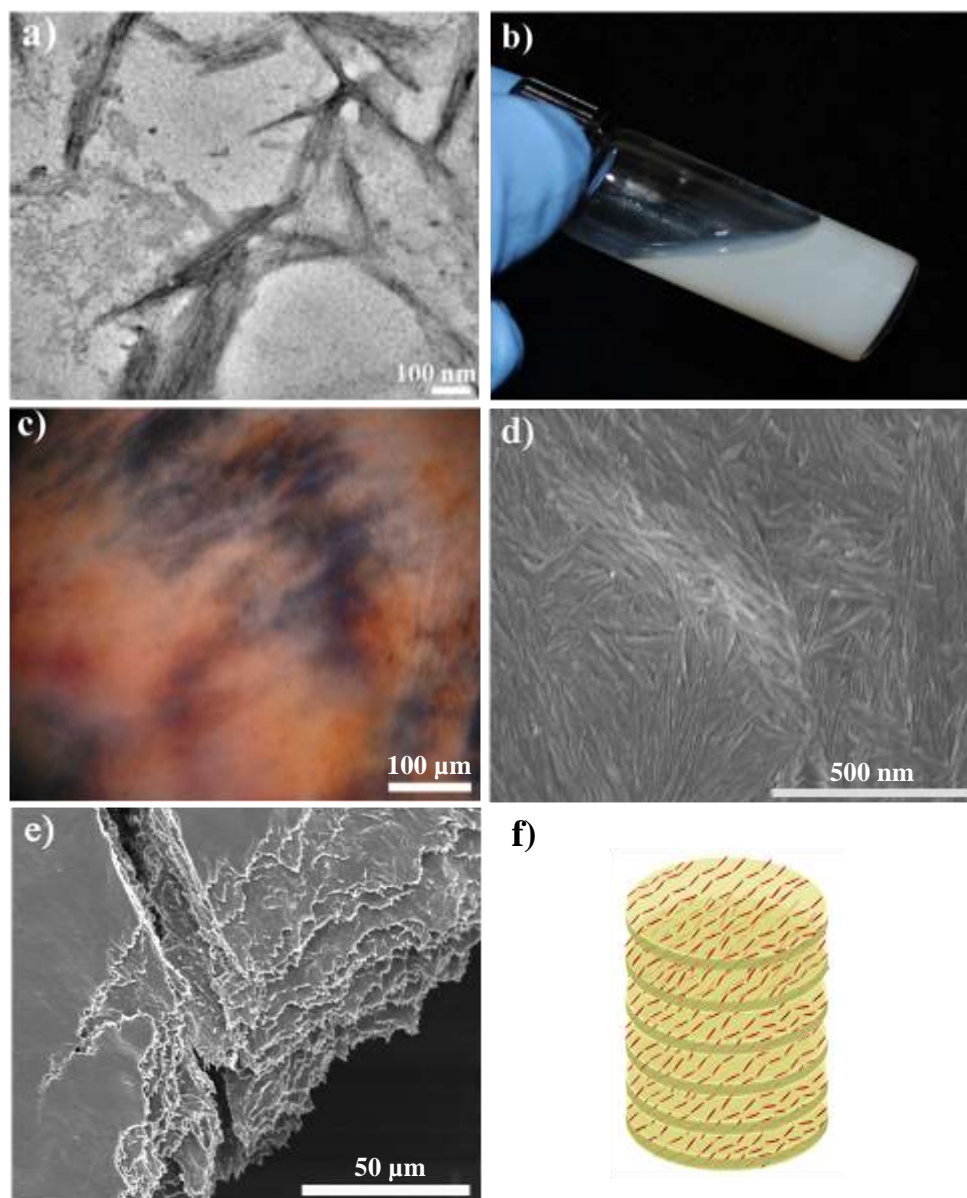


Figure S2. Nematic order of the liquid-crystalline chitin. (a) TEM image of discrete chitin nanocrystals prepared by sequential deacetylation (in 33.3 wt% NaOH at 90 °C for 2 h) and hydrolysis (in 4 M HCl at 104 °C for 18 h). (b) Vial of the aqueous NCh suspension (6.6 wt% NCh, pH ~4, $\zeta = 43.1 \pm 1.7$ mV). (c) POM image of the aqueous NCh suspension showing birefringence textures characteristic of a nematic liquid-crystalline phase. SEM images of the pure NCh films cast from the suspension viewed perpendicular to the flat surface (d) and along the edge (e). (f) Schematic illustration of the layered nematic structure of the NCh assemblies.

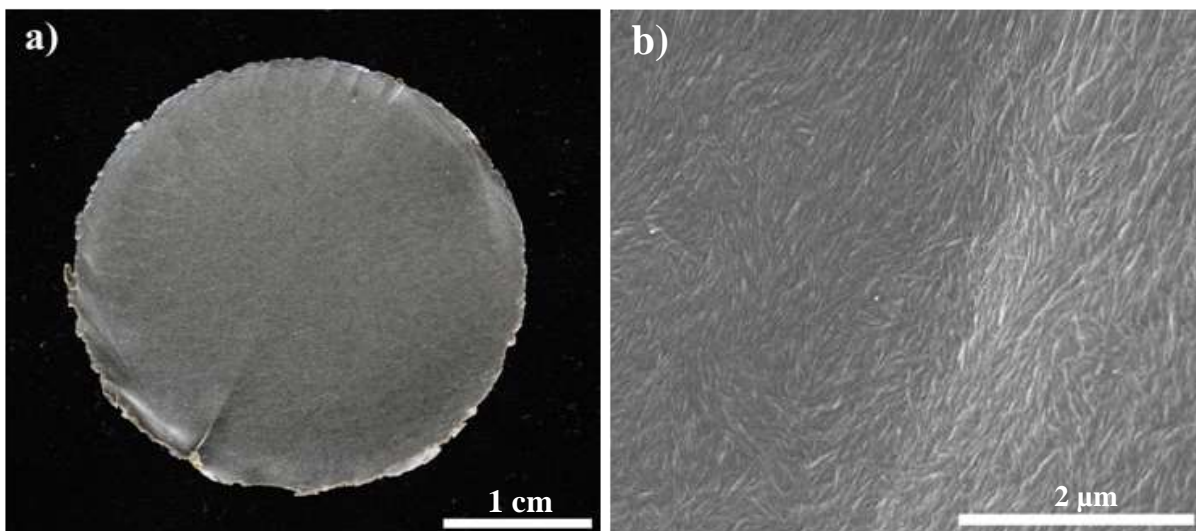


Figure S3. Sol-gel condensation of the sol-gel silica with the nematic liquid-crystalline chitin to produce silica/NCh composites (silica:NCh ratio of 23:77 wt%, assuming complete condensation). (a) Photograph of large, crack-free silica/NCh composite films and (b) SEM image viewed at top surface of the silica/NCh composites.

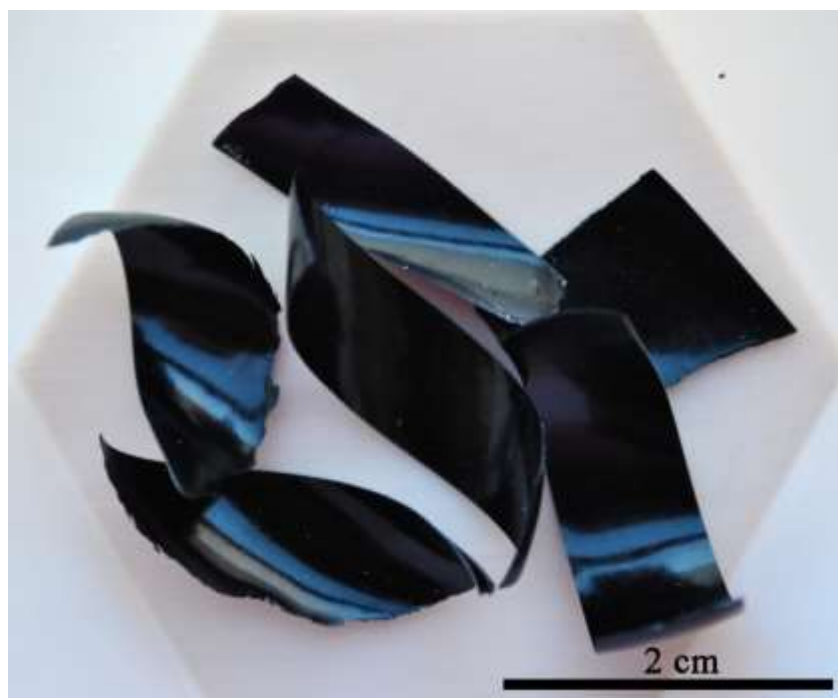


Figure S4. Photograph of the silica/nitrogen-doped carbon composites obtained from carbonizing the silica/NCh composites (silica:NCh ratio of 23:77 wt%) showing smooth surfaces and no birefringence observed under crossed polarizers due to their intensive light absorption; note that the silica/NCh composite films were cut into smaller pieces prior to carbonization.

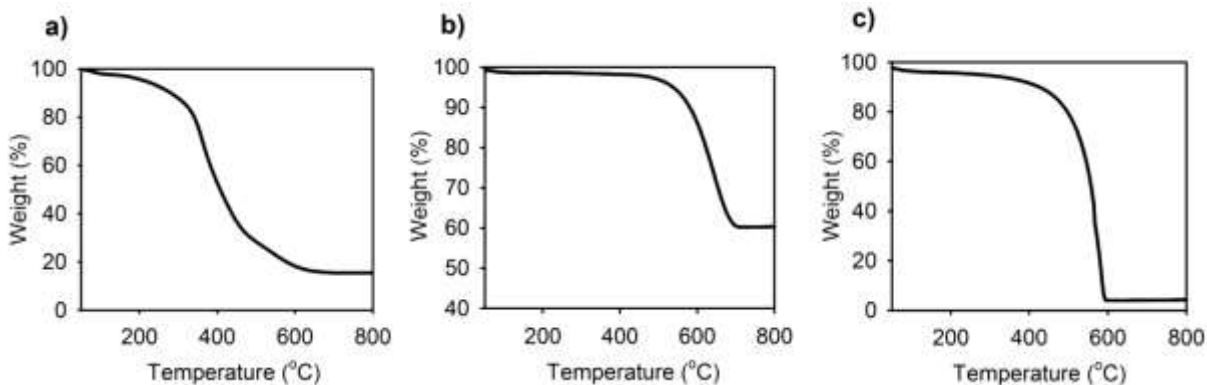


Figure S5. Thermogravimetric (TGA) curves of the composite materials and corresponding mesoporous nitrogen-doped carbon. (a) Silica/NCh composites used to generate **NC-3**. (b) Silica/nitrogen-doped carbon composites used to generate **NC-3**. (c) Mesoporous nitrogen-doped carbon **NC-3**.

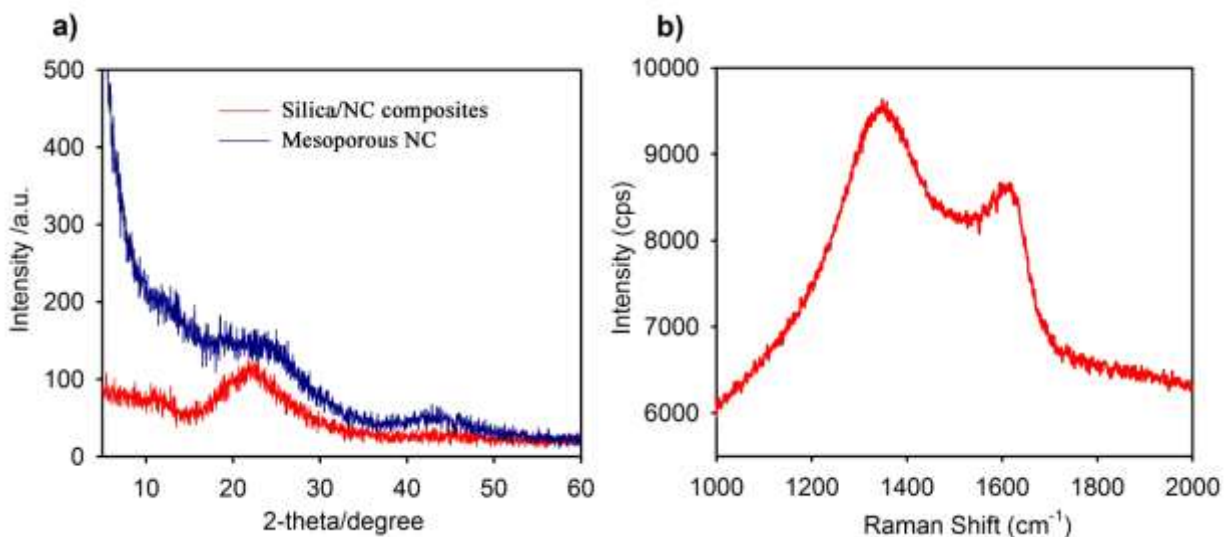


Figure S6. (a) Powder X-ray diffraction (PXRD) patterns of the silica/nitrogen-doped carbon composites and corresponding mesoporous nitrogen-doped carbon (**NC-3**) and (b) Raman spectrum of **NC-3**.

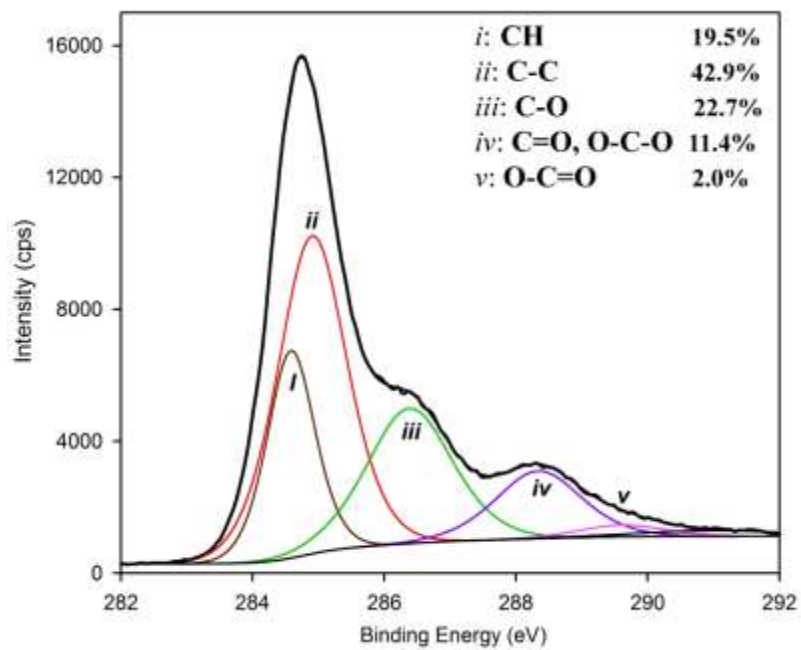


Figure S7. Deconvoluted C 1s XPS spectrum of NC-3 showing maximum peaks at 284.6 eV for CH_x and at 284.9 eV for C characteristic of graphitic carbon, and minor contributions at 286.4, 288.3, and 289.6 eV assigned to carbon bound to oxygen.⁴

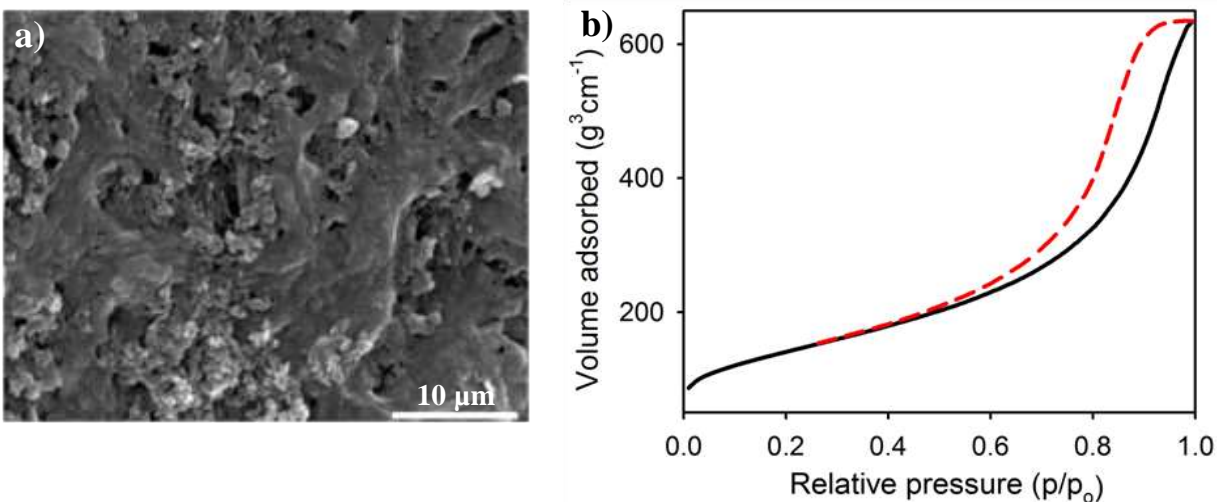


Figure S8. Mesoporous nitrogen-doped carbon from disordered chitin nanocrystals prepared by HCl-catalyzed hydrolysis of chitin fibrils at 90 °C for 2 h. (a) SEM image of **NC-6** showing disordered spindle-shaped features and (b) Nitrogen adsorption/desorption isotherms of **NC-6** presents type-IV/H3 hysteresis characteristic of a mesoporous structure with BET surface area of 506 m² g⁻¹ and high microporosity ($S_{\text{micropore}} = 120 \text{ m}^2 \text{ g}^{-1}$). Comparing the mesoporosity of **NC-3** with **NC-6** shows a transition from type-IV/H2 to type-IV/H3 hysteresis resulting from the use of the disordered NCh.

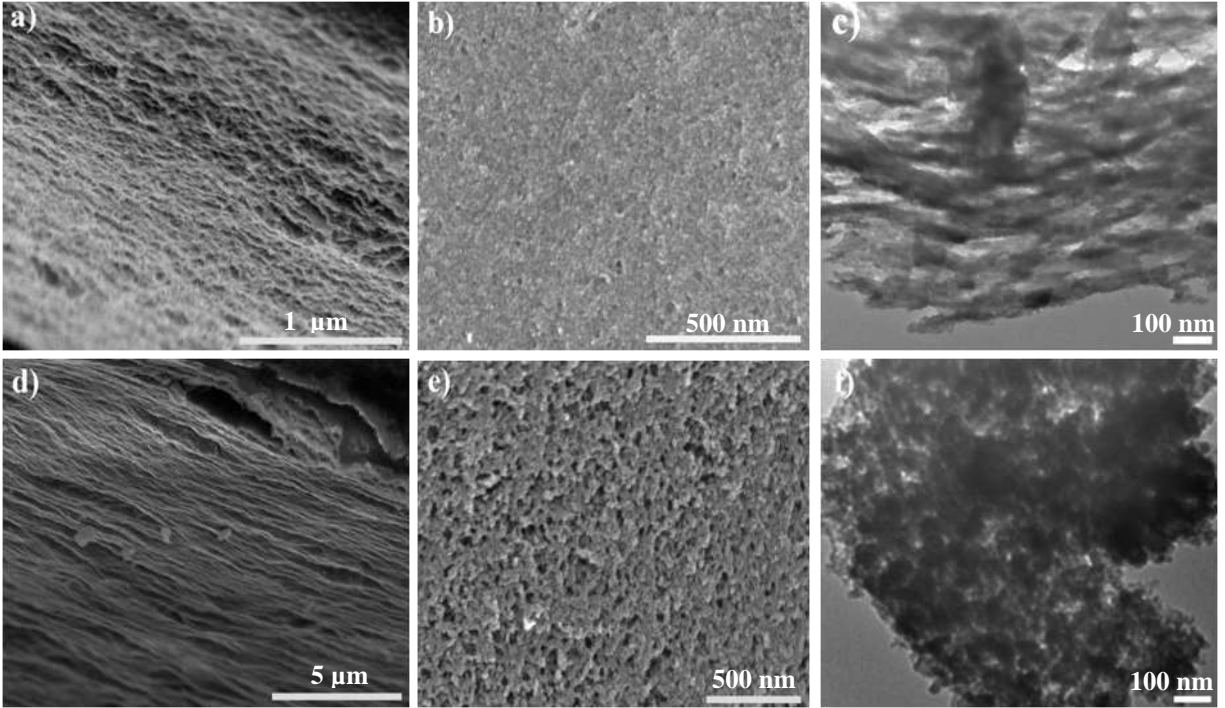


Figure S9. Effect of the fraction of the sol-gel silica in the silica/NCh composites on the nematic order of the mesoporous NC:

- NC sample prepared with low silica loading (17 wt%): SEM images of **NC-2** viewed along (a) edge and perpendicular to (b) flat surface and (c) TEM image of **NC-2** showing partial collapse of the carbon rods.
- NC sample prepared with high silica loading (33 wt%): SEM images of **NC-4** viewed along (d) edge and perpendicular to (e) flat surface and (f) TEM image of **NC-5** showing the nanospindles separated by relatively large holes resulting in the decreased interconnectivity between carbon regions.

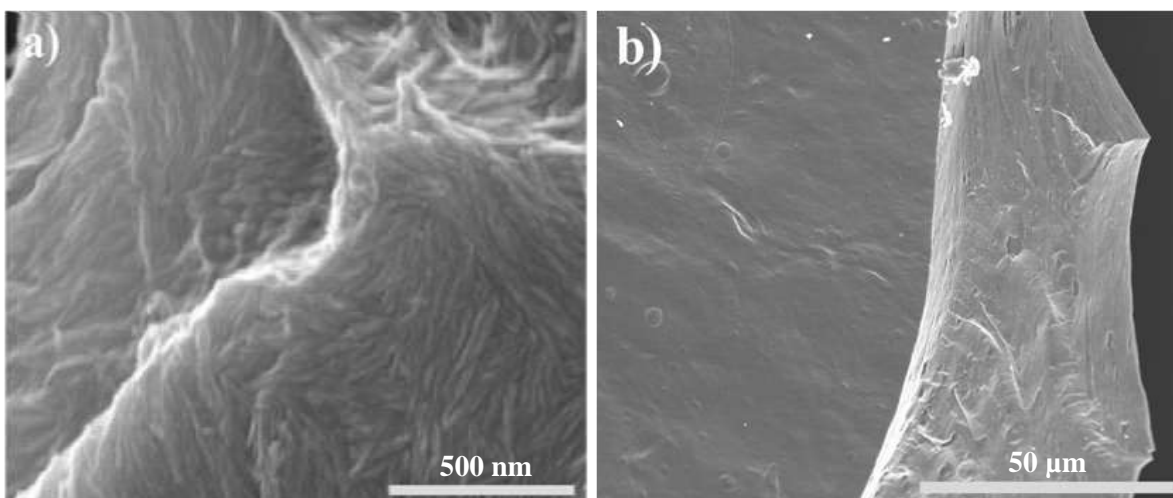


Figure S10. Carbonization of pure NCh films to produce porous nitrogen-doped carbon with very low surface area. (a) SEM image of the NCh films (before carbonization) showing a layered nematic organization of the chitin nanorod assemblies prepared by using sequential deacetylation and hydrolysis. (b) SEM image of **NC-1** produced by carbonizing the layered nematic NCh films showing a disappearance of the layered nematic features resulting from the collapse of the chitin nanocrystals upon carbonization.

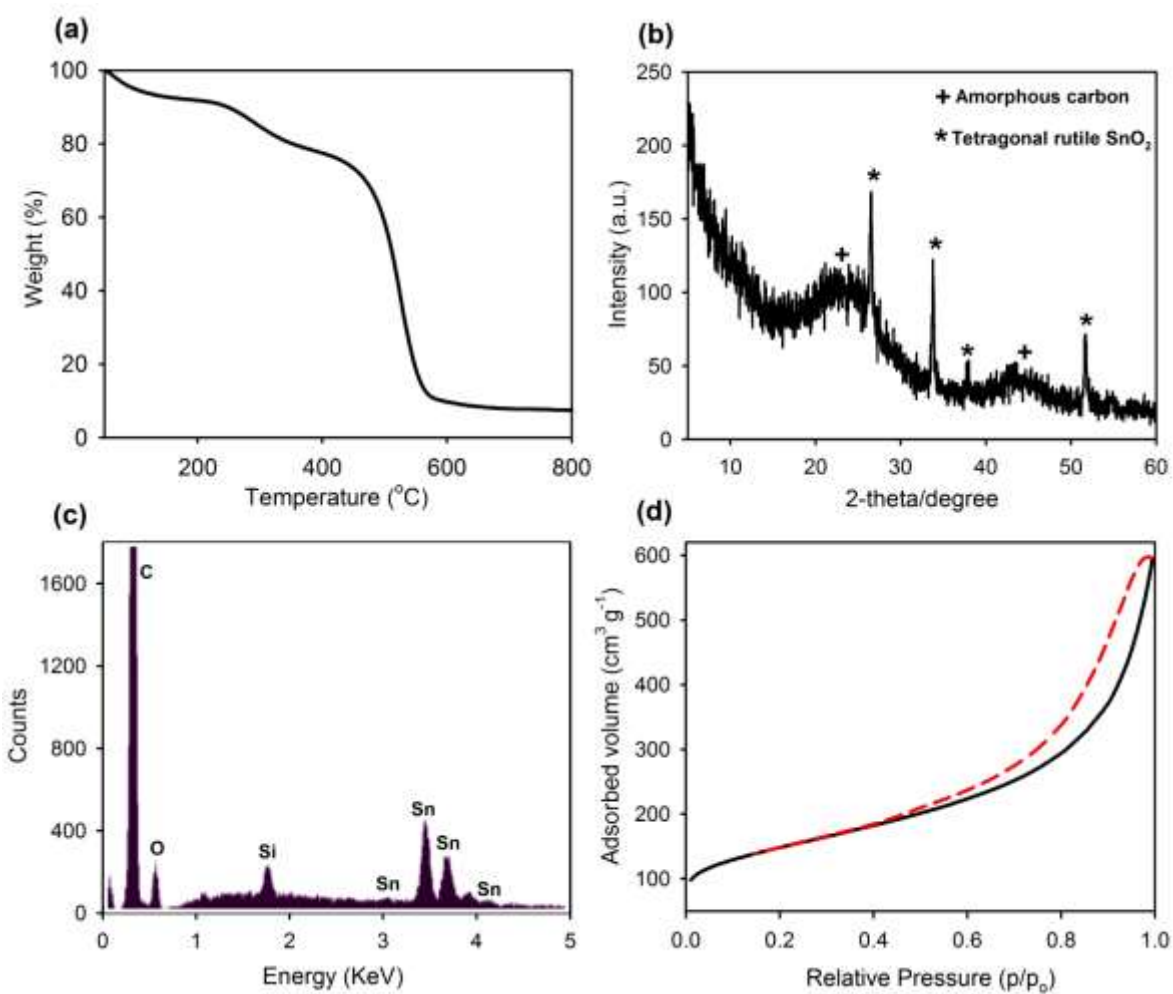


Figure S11. (a) TGA curve, (b) PXRD pattern, (c) EDX spectrum, and d) nitrogen adsorption/desorption isotherms of 5.4 wt% tin oxide-embedded nitrogen-doped carbon (TNC).

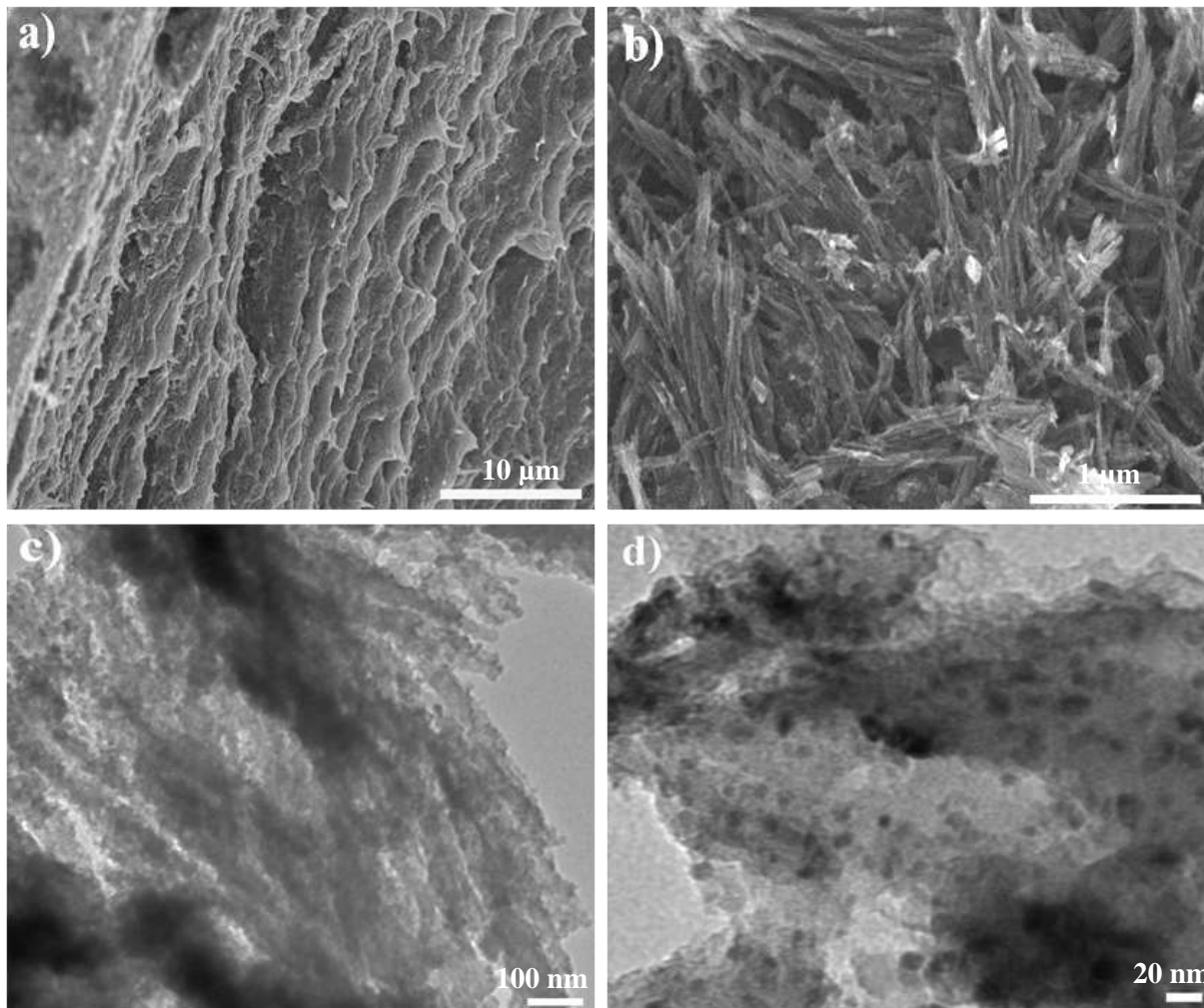


Figure S12. SEM images of the tin oxide-embedded nitrogen-doped carbon (**TNC**) viewed along edge (b) and perpendicular to broken top surface (b). (c,d) Different-magnification TEM images of **TNC**.

The structure of the **TNC** films with initial tin loading of 10 wt% Sn was verified by multi-techniques as shown in Figures S11,12. PXRD patterns of **TNC** show two separate phases of amorphous carbon and tetragonal rutile SnO_2 ,⁵ proving the conversion of the tin chloride salts to SnO_2 upon carbonization. Raman spectra of the SnO_2 -embedded NC materials resemble those of the NC samples (data not shown). EDX spectra detected ~5.4 wt% of the SnO_2 particles embedded within the NC samples after etching of the silica in accordance with TGA analysis. These results indicate that a significant amount of the tin loading was lost in the etching step of the silica. As observed in SEM images viewed at broken top surface of the **TNC** films, the

layered structure remained intact. Nitrogen adsorption/desorption isotherms of TNC show type-IV/H3 hysteresis with an decrease of the BET surface area ($\sim 527 \text{ m}^2 \text{ g}^{-1}$) and pore size distribution ($\sim 2.4 \text{ nm}$) compared to those of NC-3, probably due to pore blockage of the SnO_2 particles inside the carbon arrays. TEM images show $\sim 10 \text{ nm}$ -diameter sized SnO_2 particles deposited on the carbon arrays.

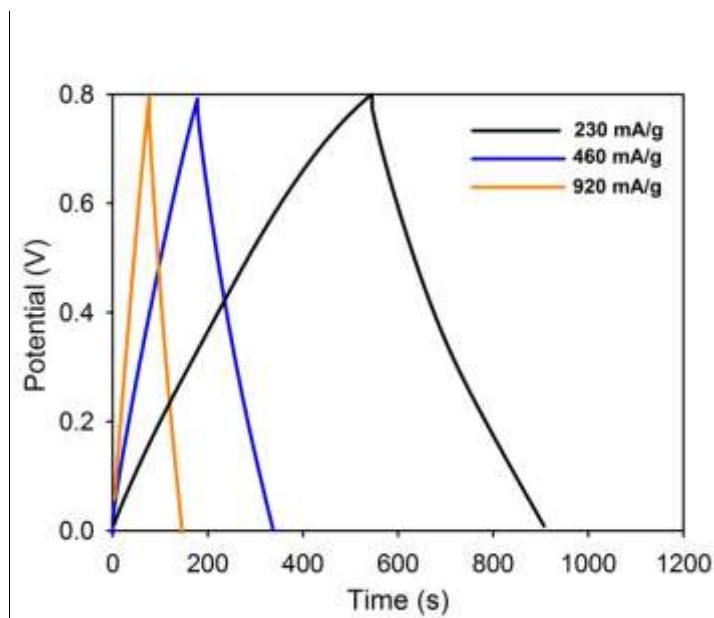


Figure S13. Galvanostatic charge/discharge curves of TNC supercapacitor electrodes in 1 M H_2SO_4 recorded at the different current densities.

References

- (1) T. D. Nguyen, Shopsowitz, K. E.; MacLachlan, M. J. *Chem. Eur. J.* **2013**, *19*, 15148.
- (2) Schroeder, D. K. *Semiconductor Material and Device Characterization*, Wiley **1990**.
- (3) Ifuku, S.; Nogi, M.; Abe, K.; Yoshioka, M.; Morimoto, M.; Saimoto, H.; Yano, H. *Biomacromolecules* **2009**, *10*, 1584.
- (4) Moulder, J. F.; Stickle, W. F.; Sobol, P. E.; Bomben, K. D. *Handbook of X-ray photoelectron spectroscopy*; Perkin-Elmer Corporation, Physical Electronics Division, **1992**.
- (5) Hwang, S. W.; Hyun, S. H. *J. Power Sources* **2007**, *172*, 451.